Radiative impacts of the Australian bushfires 2019-2020 - Part 2: Large-scale and in-vortex radiative heating

Pasquale Sellitto[1,2], Redha Belhadji[1], Juan Cuesta[1], Aurélien Podglajen[3], Bernard Legras[3]

[1] Univ. Paris Est Créteil and Université de Paris, CNRS, Laboratoire Interuniversitaire des Systèmes Atmosphériques, Institut Pierre Simon Laplace, Créteil, France
[2] Istituto Nazionale di Geofisica e Vulcanologia, Osservatorio Etneo, Catania, Italy
[3] Laboratoire de Météorologie Dynamique, UMR CNRS 8539, École Normale Supérieure, PSL Research University, École Polytechnique, Sorbonne Universités, École des Ponts PARISTECH, Institut Pierre Simon Laplace, Paris, France

Correspondence to: Pasquale Sellitto (pasquale.sellitto@lisa.ipsl.fr)

Abstract. Record-breaking wildfires ravaged south-eastern Australia during the fire season 2019–2020. The intensity of the fires reached its paroxysmal phase at the turn of the year 2019–2020, when large pyro-cumulonimbi developed. Pyro-convective activity injected biomass burning aerosols and gases in the upper-troposphere—lower-stratosphere (UTLS), producing a long-lasting perturbation to the atmospheric composition and the stratospheric aerosol layer. The large absorptivity of the biomass burning plume produced self-lofting of the plume and thus modified its vertical dynamics and horizontal dispersion. Another effect of the in-plume absorption was the generation of compact smoke-charged anticyclonic vortices which ascended up to 35 km altitude due to diabatic heating. We use observational and modelling description of this event to isolate the dominant Southern-Hemispheric biomass burning aerosol plume from the main isolated vortex. Entering this information into an offline radiative transfer model, and with hypotheses on the absorptivity and the angular scattering properties of the aerosol layer, we estimate the radiative heating rates (HR) in the plume and the vortex. We found that the hemispheric-scale plume produced a HR of 0.08±0.05 K/d, which is strongly dependent on the assumptions on the aerosol optical properties and then on the plume ageing, in our simulations. We also found in-vortex HR as large as 15-20 K/d in the denser sections of the main vortex (8.4±6.1 K/d on average in the vortex). Our results suggest that radiatively-heated ascending isolated vortices are likely dominated by small-sized strongly absorbing black carbon particles. The hemispheric-scale and in-vortex HR estimates are consistent with the observed ensemble self-lofting (a few km in 4 months) and the main isolated vortex rise (~20 km in 2 months). Our results also put in evidence the importance of longwave emission in the net HR of biomass burning plumes.

1 Introduction

Anthropogenic climate change has likely increased the occurrence of favourable conditions for the development of high-intensity wildfires (e.g., Duane et al., 2021), especially in sensitive areas like Australia (Canadell et al., 2021). Associated with an extended period of extreme heat and drought, exceptionally large bushfires developed in Australia during the 2019–

2020 wildfire season, which burnt an unprecedented area of 5.8 million hectares of broadleaf forest (Boer et al., 2020). The intensity of the wildfires escalated in south-eastern Australia during late 2019, until the development of deep pyro-convection and the formation of pyro-cumulonimbus clouds (pyroCb) that injected a large amount of gaseous and particulate pollutants in the upper-troposphere—lower-stratosphere (UTLS), producing the largest perturbation on the UTLS composition by a wildfire on record (e.g., Khaykin et al., 2020, Kloss et al., 2021, Solomon et al., 2022). The injected smoke aerosol mass in the UTLS, while quite uncertain in its total amount, might have reached values larger than 2 Tg (Hirsch and Koren, 2021), thus producing the largest known wildfire-driven perturbation of the stratospheric aerosol layer, in terms of the stratospheric aerosol optical depth (SAOD) (e.g., Khaykin et al., 2020). As an example, a monthly average stratospheric AOD up to 0.014 was observed on February 2020 at Southern Hemispheric midlatitudes by OMPS-LP (at 675 nm), which is about than ten times larger than background conditions (Sellitto et al., 2022, hereafter referred to as S22).

The large amount of solar-radiation-absorbing biomass burning aerosol injected in the stratosphere by the Australian fires in 2019-2020 produced exceptional radiative effects. A first radiative effect was the reduction of the incoming solar radiation, due to the wildfire plume, at the Southern hemispheric scale, which induced a significant radiative forcing (RF). Different contrasting estimates, in terms of the magnitude and even the sign, were given for the RF associated with the Australian fires 2019-2020. In S22 we reconciliate these different estimates and we show that their variability can be easily attributed to two main factors: 1) the uncertainty on the optical properties of the aerosol, and 2) the presence of clouds underneath the biomass burning plumes. For the first point, in S22 we argue that the optical properties of biomass burning aerosol plumes can change dramatically due to atmospheric ageing and the evolution from more to less radiation-absorbing aerosols in the shortwave (SW) spectral range, due to secondary aerosol formation and/or smoke aerosol coating/hydration. At clear-sky conditions, our best estimate, considering these evolution factors, was a global mean RF of -0.35±0.21 at top-of-atmosphere (TOA) and -0.94±0.26 at the surface. The negative RF switches to positive values if considering large black carbon (BC) particles (so with limited atmospheric ageing, as done in most atmospheric models, see Brown et al., 2021) and, to a larger extent, in case of cloud-covered scenarios or other highly reflective underlying surfaces. A second radiative effect was the generation of stable self-maintained smoke-containing anticyclonic vortices, which were observed rising well into the stratosphere, from the initial injection heigh at about 17 km up to about 35 km altitude (Khaykin et al., 2020; Kablick III et al., 2020). The existence, maintain and ascent in the stratosphere of these vortices was attributes to the diabatic heating of the airmasses due to the absorption of solar radiation in biomass burning aerosols. This very peculiar radiation-vertical-dynamics interaction, retrospectively also observed in Canadian fires in 2017 (Lestrelin et al., 2021), is not yet completely understood and is matter of theoretical studies. Beyond localised rising effects of compact isolated plumes due to radiation absorption, it was also suggested that the large-scale (Southern-Hemispheric) plume from the Australian fires 2019-2020 rose as a whole due to radiation-absorption-driven self-lofting (Yu et al., 2021).

In this paper, we use the hybrid observations/modelling methodology described by S22 to estimate the radiative heating in the aerosol plume associated with the Australian fires 2019-2020, which complements the RF estimates of S22 to cover both radiative effects mentioned previously. In particular, we estimate here, for the first time, the heating rates (HR) of both the

65   hemispheric plume and the main detached rising vortex, and we discuss, as done by S22 for the TOA and surface RF, the sensitivity of these HR estimations to the ageing of the biomass burning aerosol and resulting variability of their optical properties. We also discuss notably the concurrent role of longwave (LW) and shortwave (SW) effects, which is particularly important for HR estimations.

This paper is structured as follows. Section 2 describes the data and methods used in this work and introduces the basis of
70   offline radiative transfer modelling applied to HR estimations. Section 3 presents the observed hemispheric and in-vortex perturbation of the UTLS aerosol layer, which is key input to our RF estimates. Section 4 presents and discusses our new RF estimates. Conclusions are drawn in Sect. 5.

2 Data and methods

2.1 Offline radiative transfer modelling driven by observations

75 As discussed in S22, the idea behind our radiative impact estimation approach is to describe aerosol layer perturbations associated with a specific pollution source – the Australian fires 2019-2020, in this paper – with the best available observations and to pass this description as input to a detailed offline radiative transfer model. This approach mixes the flexibility of offline radiative transfer modelling and the realism of observations-based forcing source description. These offline radiative estimations contrast with the more widespread use of online aerosol-radiation modelling, where a point

80 pollution source is described within an atmospheric model and its radiative impact is estimated with simplified radiative models. The scheme of the offline radiative transfer approach used in this work is outlined in Fig. 1.
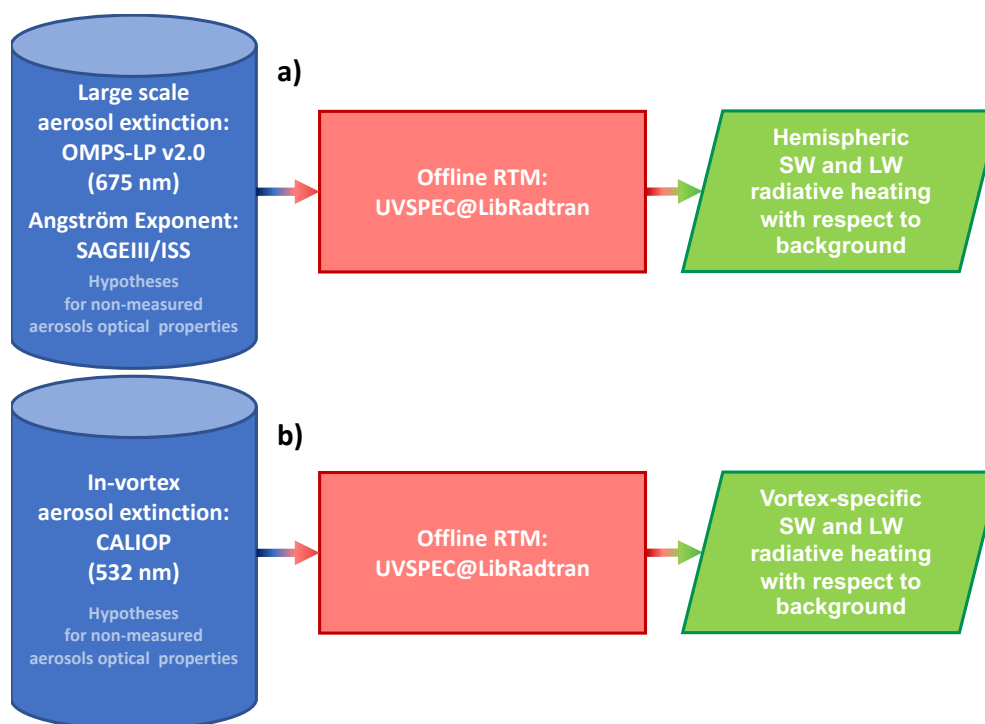
Figure 1: Scheme of the offline radiative transfer modelling used in this work for both large scale (panel a) and small-scale studies (panel b).

85 As a complement to the SW radiative forcing (RF) estimations at surface and TOA discussed in S22, in the present paper we estimate the vertically-localised radiative effects associated with the radiative interactions within the Australian wildfire plume by means of the equinox-equivalent daily-average radiative diabatic heating, as heating/cooling rates (hereafter just referred to heating rates, HR, with negative values in case of cooling). As discussed in the following sections, both the biomass burning aerosol absorption of radiation in the SW (heating rate) and emission of radiation in the LW (cooling rate)

90 are important in the HR, so both wavelength ranges are addressed in this work. To describe the radiative interaction at the

basis of both the overall self-lofting of the plume at the hemispheric scale and the more intense localised diabatic heating at the basis of the compact anticyclonic vortices first described by Khaykin et al. (2020), we present here two studies, at both the hemispheric and the in-vortex spatial scales. These two studies require a different observation-based description of the plumes as input to the offline modelling (see panels a and b in Fig. 1).

95 For the description of the overall plume at the southern hemispheric scale, we use the same inputs as done in S22 for the estimation of the surface and SW TOA radiative forcing in clear-sky conditions, which are briefly recalled in the following. A fire-perturbed scenario is obtained using monthly average OMPS-LP aerosols extinction coefficient profiles at 675 nm, for January to April 2020, at three different latitude bands (15° to 25°S, 25° to 60°S and 60° to 80°S). To cover the full spectrum of our HR estimations, a spectral variability of the aerosol extinction is represented using the observed monthly mean

100 (January to April 2020) Ångström exponent from SAGE III/ISS. The OMPS/SAGE datasets are discussed in more details in S22 and are briefly recalled in Sect. 2.2. As discussed in S22, the interaction between radiation and biomass burning aerosols cannot be fully described by the spectral aerosol extinction, which integrates the absorption and scattering processes without differentiating between them, and without describing the angular distribution of the scattered radiation. The absorption properties of the aerosol layer are particularly important for the estimation of the localised heating/cooling within the plume.

105 Unfortunately, the absorptivity and the scattering angular distribution properties of aerosol are not directly accessible from observations. Thus, we have made different hypotheses on these properties of the simulated smoke plumes, in our radiative transfer calculations. For the SW range, we adopted the same values of the aerosol absorptivity (in terms of single scattering albedo, SSA) and the angular distribution of the scattered radiation (in terms of the asymmetry parameter, g) as in S22. In particular, we made different radiative simulations with SSA values from 0.80 to 0.95 with 0.05 steps, and with g values of

110 0.50 and 0.70. Typical SSA and g values for biomass burning aerosols are not available in the LW, in the literature. To fill this gap in LW optical properties, we have performed dedicated Mie calculations, using the Mie routines of the Earth Observation Data Group of the Department of Physics of Oxford University (http://eodg.atm.ox.ac.uk/MIE/). In the Mie calculations, we have used the refractive indices of biomass burning aerosols of Sutherland and Khanna (1991) and different mono-modal log-normal size distribution with fixed width of 1.86 and varying mean radii from 0.2 to 0.6 μm. The average

115 value of the SSA in the LW was found quite stable around a value of 0.20, with small variability with respect to variability in the mean radius. The average value of g in the LW varied between a minimum of about 0.30 and a maximum of about 0.50. Thus, in the LW we made different radiative simulations with SSA value of 0.20 and with g values of 0.30 and 0.50. The SSA and g values have been considered as spectral-independent in the SW and LW spectral ranges. The plume's HR is obtained by subtracting the HR results of a background atmosphere from the HR outputs of the fire-perturbed scenario. As a

120 clean background, we have considered the respective monthly means OMPS/SAGE spectral extinction observations for the year 2019. Background UTLS values of SSA and g are considered, for typical values of sulphate aerosol, which dominate the aerosol layer at these altitudes in the absence of fire perturbations (Kremser et al., 2016). Typical values in the SW, available in the literature, were taken as SSA=0.99 and g=0.70. In the LW, an SSA of 0.20 and a g of 0.30 were obtained

with the Oxford Mie code, using sulphate aerosol refractive indices from Hummel et al., 1988 and a mono-modal log-normal
125   size distribution with width of 1.86 and mean radius from of 0.2 μm.

For the description of the more localised smoke-charged compact anticyclonic vortices, we use high vertical resolution
aerosol extinction observations with the satellite-borne LiDAR CALIPSO-CALIOP. The CALIOP datasets are briefly
discusses in Sect. 2.3. As for the hemispheric-scale HR estimations, for the localised in-vortex calculations we have made
hypotheses for the non-measured optical properties, SSA and g. More constrains on these optical properties are given by the
130   CALIOP measurements of the LiDAR ratio (LR), colour ratio (CR) and depolarisation ratio (δ), which is discussed in Sects.
3 and 4.2. As a background atmosphere, we have taken the same background as for the hemispheric-scale runs.

As offline radiative transfer model, we use the UVSPEC (UltraViolet SPECtrum) model in its libRadtran (library for
Radiative transfer) implementation (Emde et al., 2016), using the SDISORT (spherical DISORT) solver (Dahlback and
Stamnes, 1991), in the SW, and a two streams approximation in the LW. The atmospheric state is set using the AFGL (Air
135   Force Geophysics Laboratory) climatological standards (Anderson et al., 1986), as in S22.

We finally estimate SW and LW HR between surface and 50 km altitude with 1-km vertical resolution. Calculations are
realised at different solar elevations, i.e. different solar zenith angle (SZA); the equinox-equivalent daily-average SW and
LW HR are then calculated as the SZA-averaged HR, assuming that the duration of day and night is equal.

2.2 Aerosol spectral extinction observations with the Ozone Mapper and Profiler Suite – Limb Profiler (OMPS-LP)
140   **and the Stratospheric Aerosol and Gas Experiment III on the International Space Station (SAGE III/ISS)**

The spatiotemporal variability of the average large-scale fire-perturbed and the background aerosol extinction is obtained
using v2.0 aerosol extinction observations at 675 nm from the Ozone Mapping and Profiler Suite - Limb Profiler (OMPS-
LP), onboard the Suomi National Polar-orbiting Partnership (Suomi-NPP) satellite since January 2012 (Taha et al., 2020).
The OMPS-LP instrument observes scattered solar radiation at different tangent heights (from cloud-top height to 40 km,
145   with a 1-km vertical resolution), in the 290-1000 nm spectral range. Even if OMPS-LP v2.0 observes the aerosol extinction
at different wavelengths, multi-spectral analyses with this dataset are not recommended due to inhomogeneities of the
accuracy of spectral aerosol observations due to different sources of bias for each band (Taha et al., 2020). Thus, in this
work, the spectral variability of the aerosol extinction is represented using the Ångström Exponent (AE) estimated from
multi-spectral observations of the Stratospheric Aerosol and Gas Experiment III instrument, onboard the International Space
150   Station (SAGE III/ISS) since February 2017. The SAGE III/ISS instrument observes the aerosol extinction coefficient
profiles in the stratosphere with a solar-occultation geometry, thus with a much larger signal-to-noise ratio than OMPS-LP
but much smaller spatial coverage, at nine individual spectral bands from 385 to 1550 nm. As in S22, the AE used in this
paper is obtained using SAGE III/ISS aerosol extinction observations at 521 and 869 nm.

2.3 Aerosol extinction observations with the Cloud-Aerosol Lidar and Infrared Pathfinder Satellite Observation -
155 **Cloud-Aerosol Lidar with Orthogonal Polarisation (CALIPSO-CALIOP)**

High vertical and horizontal resolution observations of the CALIOP (Cloud-Aerosol Lidar with Orthogonal Polarisation) spaceborne LiDAR onboard the CALIPSO (Cloud-Aerosol Lidar and Infrared Pathfinder Satellite Observation) satellite are used for the description of the smoke-charged compact anticyclonic vortices emanating from the main Australian wildfires plumes. As a main parameter, we use attenuated aerosol backscatter profiles at 532 nm. The AOD of the vortices is estimated
160 from the ratio of the LiDAR signal at aerosol-free altitudes above and below their optical signature. Aerosol LiDAR ratios LR are roughly calculated by dividing the AODs by the vertically integrated attenuated backscatter after subtracting molecular backscatter. Finally, LR are used for calculating aerosol extinction profiles using a classic LiDAR equation (Fernald, 1984). Observations of the backscatter profiles at 1064 nm are used, in combination with the channel at 532 nm, to obtain a colour ratio parameter CR, which is an optical proxy of the mean particle size in the aerosol layer. Information on
165 the polarisation state of the backscatter radiation is also obtained in the channel at 532 nm as a depolarisation ratio δ, which brings critical information on particle shape.

The main detached vortex is tracked using ECMWF (European Centre for Medium-Range Weather Forecasts)-IFS (Integrated Forecasting System) reanalyses. As done by Khaykin et al. (2020), ECMWF-IFS-derived datasets of vorticity and ozone anomalies are used as vortex tracers. In this work, these datasets are used to identify CALIOP overpasses of the
170 main detached vortex from Australian bushfires.

3 The hemispheric plume and the vortex

The hemispheric perturbation of the stratospheric aerosol layer by the Australian wildfires 2019-2020 is discussed in detail in S22. Here we show further specific observations of the double manifestation of the overall aerosol perturbation from this event, the hemispheric-scale plume and the detached compacts vortices. While the large-scale plume is observable with limb
175 observations at all latitude bands (S22), the detached vortices are more difficult to characterise with this observation geometry, due to their relatively small horizontal size and because of their relatively rapid horizontal paths across the Southern Hemisphere. Khaykin et al. (2020) provided a detailed reconstruction of the horizontal dynamics of the main vortex by means of ECMWF-IFS reanalyses and different satellite observations, showing that most of the signature of the main vortex can be found in the latitude band between approximately 35 and 50°S (see e.g. their Fig. 6). Figure 2a shows
180 time series of the zonal average vertical distribution of the OMPS-LP aerosol extinction at 675 nm in the latitude band 40-45°S, which displays clear evidence of both the large-scale plume and the main detached vortex. Both features display a self-lofting behaviour. The overall effect of the plume rise can be seen in January and February 2020, with progressively higher altitude of the dominant aerosol optical signature, from the injection height at about 17 km up to 20-21 km. The isolated and shorter-term signature of the main vortex, when it vertically separates from the main plume, is clearly visible from February
185 to beginning March, with aerosol extinction enhancements exceeding 30 km altitude. While the zonal average aerosol

extinction is clearly dominated by the hemispheric plume below ~22 km, values exceeding 10^{-3} to 10^{-2} km^{-1} are associated with the main vortex at higher altitudes. To show this latter effect, Fig. 2b shows the OMPS-LP aerosol extinction coefficient, in the latitude band 40-45°N, at a fixed altitude of 28 km. The presence of the vortex produced a transient (about two weeks) increase of the aerosol extinction at this altitude of at least 2-3 order of magnitude with respect to background

190   conditions. A following longer lasting (until August 2020) perturbation of the aerosol extinction, at these altitudes, is also visible in Fig. 2b (see also corresponding period in Fig. 2a); its origin is not yet fully understood and matter of future work. The double nature of the aerosol perturbation by the Australian wildfires is also visible from the monthly average extinction profiles, see, e.g., February 2020 average in Fig. 2c. The mutual magnitude of the hemispheric plume (at approximately 15 to 22 km altitudes) and the vortex (at approximately 25 to 30 km altitudes) can be appreciated from this figure.
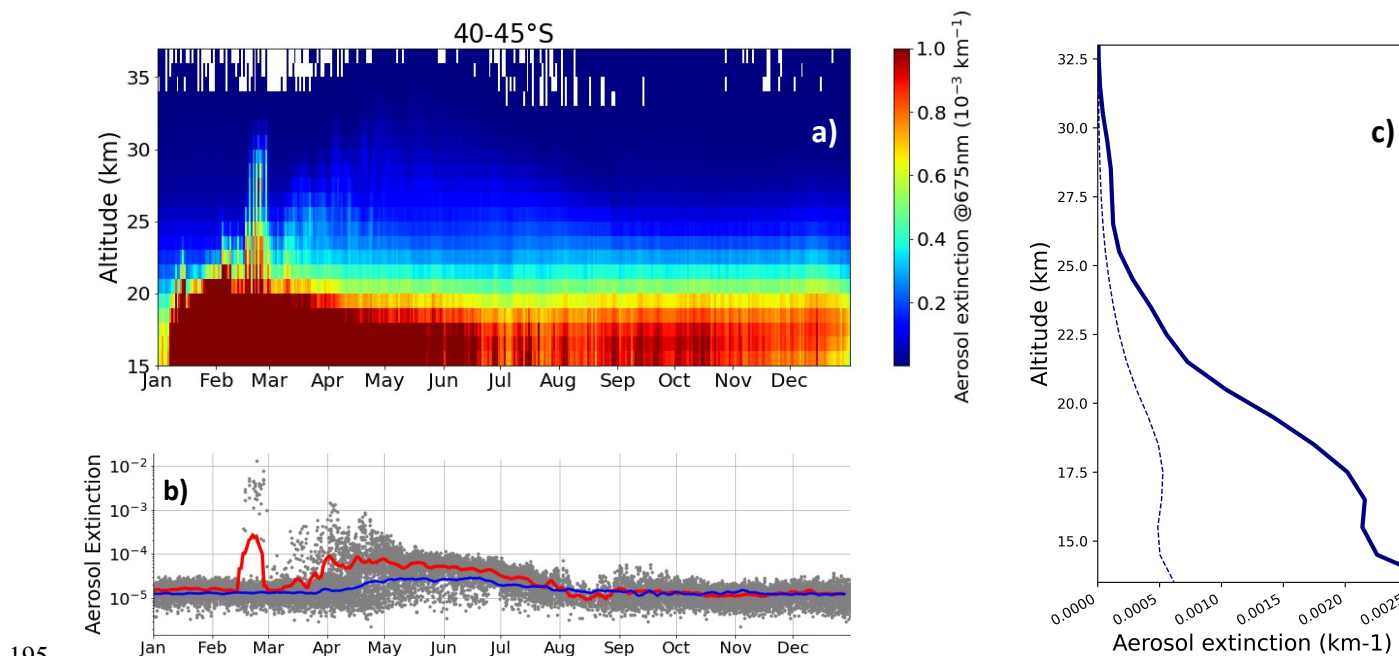
Figure 2: OMPS-LP observations at 675 nm in the latitude interval 40-45°S: time series of the zonal average vertical profiles of the aerosol extinction in 2020 (panel a), individual aerosol extinction coefficient observations at 28 km altitude (panel b), monthly mean aerosol extinction coefficient profiles in February 2020 (perturbed profiles, solid lines) and February 2019 (background profiles, dashed lines) (panel c). In panel b, temporally smoothed time series for 2020 (red curve) and 2019 (blue curve) are also
200   **shown.**

High vertical resolution observations of the main vortex emanating from the Australian fires 2019-2020 are available with in-vortex CALIOP observations. In Fig. 3, an example these observations is shown for 11 January 2020. Using dynamical information taken from ECMWF-IFS vorticity, it can be seen that one CALIOP track overpassed the vortex near its centre, during this day (Fig. 3c). The vortex is also accompanied by a dynamically driven ozone mini-hole, as described by Khaykin

205   et al. (2020), thus ozone mixing ratio anomalies can also be used to track the vortex position (see Fig. 3d). The morphology and magnitude of the aerosol signature associated with the vortex are shown in Fig. 3a-b, by means of vertical profiles of the attenuated backscatter and the aerosol extinction. During this early stage of its lifetime, the vortex was located around 17-22

km altitude, with a maximum of the aerosol extinction and potential vorticity at 19-22 km. The frontal structure of the vortex (see magenta section in Fig. 3a-b) and the leaking of smoke aerosols at lower altitudes (see green section in Fig. 3a-b) are

210 clearly visible for this overpass. These two aspects of the plume morphology and dynamics are described in detail by Podglajen et al. (2023). The CALIOP instrument allows further characterisation of the sampled aerosol type through different optical parameters, like the AOD and depolarisation, color and LiDAR ratios (δ, CR and LR, optical proxies of particles sphericity, mean size and type, respectively). The mean values of these optical parameters, for the core vortex (magenta section in Fig. 3a-b), together with other typical values of aerosol, ozone and dynamical parameters taken by

215 CALIOP observations and ECMWF-IFS reanalyses, are listed in Tab. 1. The first thing to be noted is the extremely large AOD for the vortex, at this early stage, with an average value in the vortex core of ~0.65 and a peak value of ~0.80, in the visible range. A relatively large LR, ~76 sr in our case, is found, which is typical of biomass burning aerosols (e.g. Burton et al., 2013). Usually, aged biomass burning aerosols are also associated with relatively small δ and large CR (e.g. Papagiannopoulos et al., 2018), which in turns point at spherical and small particles. On the contrary, during our overpass,

220 the average value of δ is about 12%, which can be associated to significantly aspherical particles and CR is about 0.7, which can be associated with relatively large particles. These results point at a very dense layer of extremely fresh biomass burning particles, i.e. with large ash that has not yet sedimented and before significant hydration and secondary aerosol formation (the processes that tend to render the biomass particles more spherical). This points to absorbing black-carbon-dominated aerosol layers. In S22, we have shown evidence that the hemispheric plume for the Australian fires 2019-2020 may have

225 undergone atmospheric evolution towards less absorbing brown carbon particles. Thus, we expect that the optical properties of the large-scale plume and the vortices are significantly different, possibly due to the isolation of these latter from ambient air.
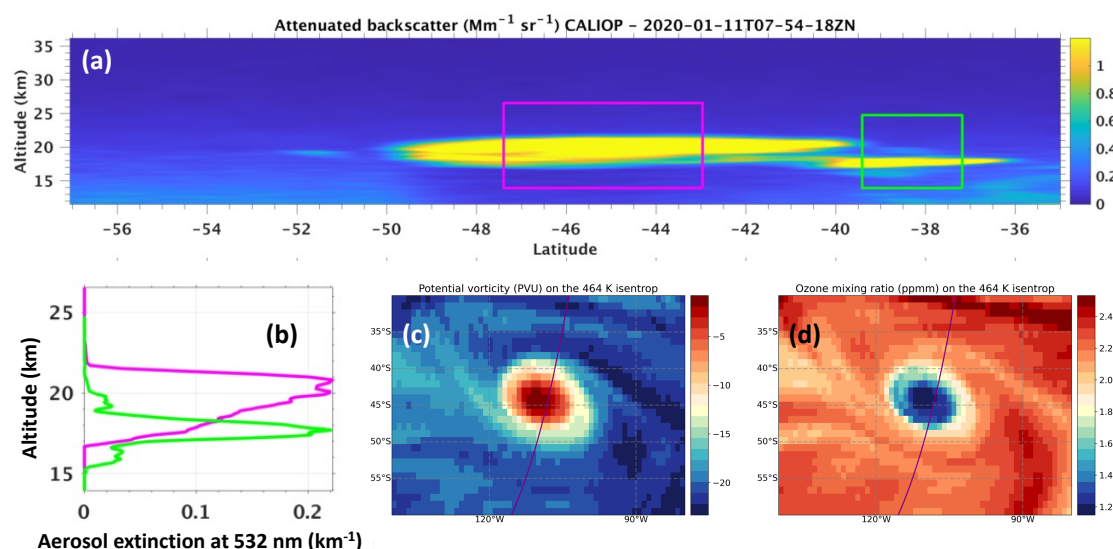
Figure 3: CALIOP attenuated backscatter observations at 532 nm for the main vortex overpass of 11 January 2020 (panel a) and
230 **aerosol extinction profiles averaged in the magenta and green boxes individuated in panel a, in respective colours (panel b). The**

CALIOP overpass of the vortex, individuated by means of ECMWF-IFS potential vorticity and ozone mixing ratio anomalies, is shown as the violet track in panel c and d, respectively.

Table 1: Morphological and optical properties of the vortex individuated in Fig. 3 for 11 January 2023, from CALIOP observations and ECMWF-IFS reanalyses.

Approximate altitude	**17-22 km**
Altitude of maximum potential vorticity	**19.5 km**
Maximum ozone anomaly	**-1.2 ppm**
Altitude of maximum aerosol extinction	**20-21 km**
Mean aerosol extinction (17-22 km)	**~0.10 km^{-1}**
Maximum aerosol extinction	**~0.21 km^{-1}**
Mean AOD (magenta plume in Fig. 3a)	**~0.65**
Maximum AOD	**~0.80**
Mean depolarisation ratio	**~12%**
Mean colour ratio	**~0.7**
Mean LiDAR ratio	**75.8 sr**

235

4 Radiative heating

4.1 Large scale HR and sensitivity to aerosol optical properties

An aerosol layer interacts with solar and terrestrial radiation, leading to modifications to the net radiation fields at surface and TOA (the surface and TOA RF) of interest for the radiative balance and climate, depending on the optical properties of

240 the aerosol layer. For the aerosols emitted during the Australian fires 2019-2020, this effect is discussed in detail by S22. Besides this, an aerosol layer can also modify the local energy budget, introducing a radiatively-driven diabatic heating or cooling. Temperature increases or decreases can then be generated due to the excess of absorbed or emitted radiation, which can in turns modify the vertical dynamics lofting or sinking air masses. This radiative impact can be quantified with radiative

heating and cooling rates as a function of the altitude. In this paper, we use the idea of negative HR to address cooling rates.

245   Like for the surface and TOA RF, the HR depend critically on the optical properties of the aerosol layer. These can be defined in a compact way by quantifying their overall extinction (by means of the aerosol optical depth, AOD), their absorption properties (by means of their single scattering albedo, SSA) and angular distribution of the scattered radiation (by means of their phase function, synthesised with the asymmetry parameter, g). Please see S22 for more details and discussion on these properties.

250   A simple expression of the HR is given in Eq. 1 (Liou, 2002). In this equation, ρ is the air density, C_p is the air heat capacity at constant pressure, $\Delta F(z)/\Delta z$ is the variation of the net radiation flux due to the presence of a specific forcing agent, the aerosol plume from the Australian fires, in our case. For an aerosol layer, the net radiation flux modification $\Delta F(z)$ depends critically on its optical properties, which transmits this dependency to the HR. How the HR depend on the optical properties of an aerosol layer is still very uncertain and subject to active research, which is particularly the case for the LW component

255   (e.g. Liou, 2002).

$$HR = HR_{SW} + HR_{LW} = -\frac{1}{\rho C_p}\left(\frac{\Delta F(z)}{\Delta z}\right)_{SW} + -\frac{1}{\rho C_p}\left(\frac{\Delta F(z)}{\Delta z}\right)_{LW} \tag{1}$$

Figure 4 shows sensitivity analyses of the SW, LW and net SW+LW HR for the large-scale average aerosol plume, for the 4 months addressed in this study and for 3 latitude ranges, when using different assumptions on the SW and LW SSA and g optical parameters in our offline radiative transfer calculations. As discussed by S22, in the SW, the plume ageing is

260   expected to lead towards an increase of the SSA and g due to the progressive atmospheric evolution of small and absorbing black carbon towards larger and less absorbing brown carbon particles. Less is known about typical values of the LW SSA and g. As discussed in Sect. 2.1, we estimated LW optical parameters with a Mie code and found that the LW SSA is largely insensitive to atmospheric ageing, while LW g progresses towards larger values, as in the SW range. For both the SW and the LW spectral ranges, the HR is found largely insensitive to g. The SW HR display a marked peak of positive values in the

265   vertical region perturbed by the large-scale plume from the Australian fires, around 12-25 km altitude. The absolute value of the HR depends critically on the SW SSA, and then on the absorptivity of the layer in this spectral range, with values as large as 0.5 K/d (February average, 15-25°S) for smaller SSA, and then for more absorbing aerosols. The SW HR decrease steeply with increasing SSA, i.e. for more aged and less absorbing aerosol layers. The LW HR is generally a cooling in the vertical region perturbed by the large-scale plume, with a simultaneous heating at higher altitudes, around 35 km. The LW

270   radiative cooling in the region occupied by the Australian fires aerosols is almost independent on the atmospheric ageing processes of the aerosol layer, and has values comparable with the positive HR in the SW. As a result, the net SW+LW HR has reduced values with respect to the SW-only component, which demonstrates the importance of taking into account the LW HR component. After a transient phase in January 2022, the net HR induced by the Australian fires is generally positive (dominated by SW) and of the order of about 0.2 K/d (15-25°S and 25-60°S) and 0.1 K/d (60-80°S) on February-April 2020,

275   when averaged over the different hypotheses on SSA and g.

Starting from the regional estimates of HR, we estimate the Southern-Hemispheric HR with an area-equivalent averaging of these values. Figure 5 shows time series of the monthly mean (January to April 2020) Southern-Hemispheric HR, as a function of the different hypotheses on SSA and g, as well as an average over all scenarios. The SW and LW HR are consistently positive and negative, respectively, with a dominance of the SW heating, leading to a maximum net HR
280   (averaged over all SSA and g scenarios) of 0.08±0.05 K/d in February 2020 (SW HR: about 0.09 K/d, LW HR: about -0.02 K/d). Reflecting the evidence discussed for the regional HR estimations, the LW hemispheric HR displays a very small variability, and the SW hemispheric HR displays a very large variability, as a function of atmospheric ageing (see also error bars of the SW, LW and net SW+LW HR in Fig. 5). Due to this large variability of the SW HR, the net hemispheric SW+LW HR varies, in February 2020, between about 0.02 K/d (very reflective particles, SSA: 0.95) and 0.12 K/d (very
285   absorbing particles, SSA: 0.80). The net SW+LW HR is consistent with an ensemble self-lofting of the overall hemispheric plume of a few km in 4 months (see Fig. 2a and the inherent discussion in Yu et al., 2021). Our hybrid observations/modelling estimations are consistent with the modelling-based estimations of Heinold et al. (2022), even if slightly larger.
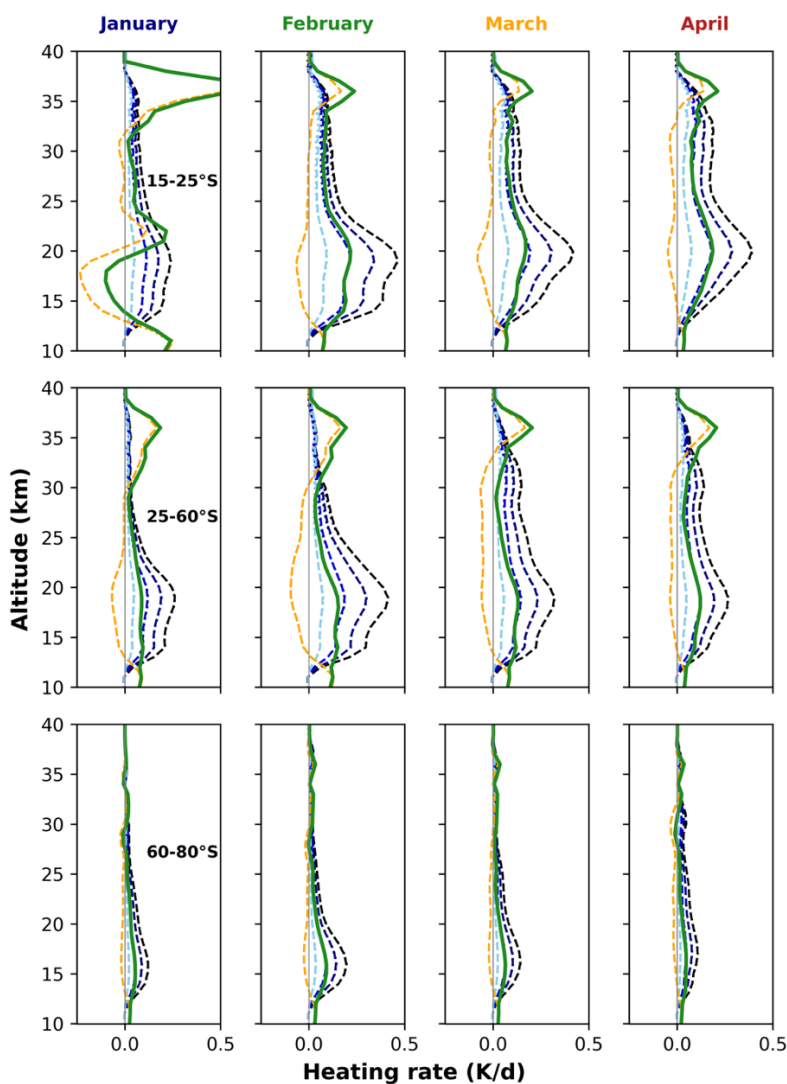
Figure 4: Monthly mean regional equinox-equivalent daily-average), SW (shades of blue and black lines), LW (orange lines) and net SW+LW (green lines) HR, from January to April 2020 (different columns), in three latitude ranges (15-25, 25-60 and 60-80°S, upper to bottom lines). Following the Mie calculations discussed in the text, different assumptions are made for SSA and g. SSA (SW component): sky blue lines: 0.95, medium blue lines: 0.90, dark blue lines: 0.85, black lines: 0.80. SSA (LW component): orange lines: 0.20. G (LW component): dashed lines: 0.5, dotted lines: 0.3. G (SW component): dashed lines: 0.7, dotted lines: 0.5.
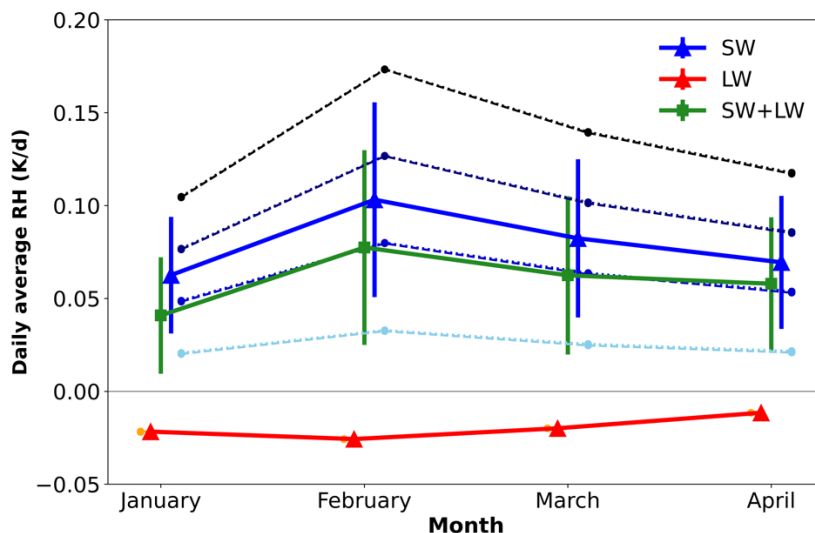
295

Figure 5: Time series, from January to April 2020, of the monthly mean area-weighted Southern-Hemispheric HR, based on equinox-equivalent daily-average HR of Fig. 4), for the UTLS perturbation of Australian fires in 2019–2020. The radiative heating profiles are averaged in the altitude range 12-25 km. Different shades/types of blue dots and lines are for different SSA and g values – the darker the shade the smaller the SSA, dashed/dotted lines for larger and smaller g, see caption of Fig. 4 for details.

300 **Different types of orange dots and lines are for different g values – dashed/dotted lines for larger and smaller g, see caption of Fig. 4 for details. The HR values, averaged over all SSA and g scenarios, for different spectral ranges are also in different colours: SW: blue triangles with error bars and lines, LW: red triangles with error bars and lines, net SW+LW: green squares with error bars and lines. The error bars are representative of the variability of the average SW, LW and SW+LW monthly means radiative heating due to SSA and g variability.**

305 **4.2 Diabatic heating and the vortex dynamics**

To get more insights into the radiative interactions within the isolated vortex features emanating from the larger scale biomass burning plume from the Australian fires, we estimated the HR in the main vortex discussed in Sect. 3. As input to our offline radiative modelling, we considered the exemplary CALIOP overpass of 11 January 2020 shown in Fig. 3. Figure 6 shows the SW, LW and net SW+LW HR for this overpass of the vortex, with 3 different scenarios of the unmeasured

310 optical properties: black carbon, large black carbon and brown carbon (consistent with the definitions given by S22, see also the caption of Fig. 6). Table 2 present average values of the HR in the full vortex-occupied vertical interval between 18 and 23 km. The observed ascent of the vortices (Khaykin et al., 2020) requires a positive diabatic heating (Podglajen et al., 2023). From Fig. 6 it is evident how the only configuration which produces the required positive HR, in our simulations, is the one associated with fresh, small, very absorbing BC particles. These conditions are possibly verified in the first couple

315 months and maintained for a relatively long time due to the dynamical isolation of the vortices. Air masses mixing with ambient air might evolve more quickly towards less absorbing particles, which would not be compatible with the enhanced ascent observed for the isolated vortices. The net HR for the BC scenario (Fig. 6a) reaches values as large as 15-20 K/d in the core of the vortex, at 20-21 km (SW HR: about 25 K/d, LW HR: about -5 K/d), and an average value of 8.4±6.1 K/d in

the overall vertical region between 18 and 23 km. These values of the HR are consistent with a vortex rise of about 20 km in

320   2 months. The large BC scenario (Fig. 6b), on the contrary produces a close-to-zero net HR (0.2±1.9 K/d, averaged between

18 and 23 km altitude), due to compensation of SW heating and LW cooling, while the BrC scenario (Fig. 6b) produces a net

cooling (-4.0±4.2 K/d, averaged between 18 and 23 km altitude). Thus, both these scenarios are inconsistent with the

observed vertical dynamics of the main vortex emanating from the Australian fires.
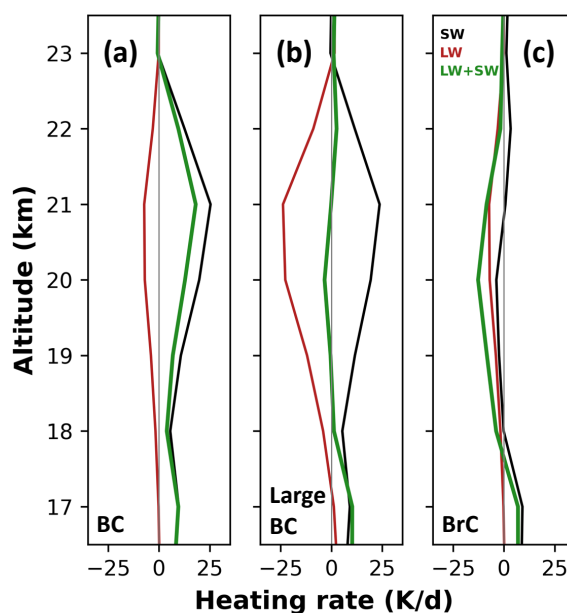
325   **Figure 6: In-vortex SW, LW and net SW+LW HR for the CALIOP overpass of the main vortex on 11 January 2020 (CALIOP overpass shown in Fig. 3), with 3 assumed scenarios for the unmeasured aerosol properties: Black carbon (BC, SW SSA: 0.80, SW g: 0.5-0.7, LW SSA: 0.20, LW g: 0.3, panel a), Large black carbon (Large BC, SW SSA: 0.80, SW g: 0.7, LW SSA: 0.20, LW g: 0.5, panel b) and Brown carbon (BrC, SW SSA: 0.90-0.95, SW g: 0.7, LW SSA: 0.20, LW g: 0.5, panel c). These 3 cases are defined in a consistent manner as in S22.**

330   **Table 2: Average HR and maximum positive/negative HR in the altitude range 18-23 km, for the 3 scenarios of Fig. 6**

	Average HR (18-23 km) (K/d)	**Maximum positive HR (K/d)**	**Maximum negative HR (K/d)**
BC	8.4±6.1	18.1	-
Large BC	0.2±1.9	2.6	-3.4
BrC	-4.0±4.2	1.1	-10.7

5 Conclusions

In this manuscript we have presented an array of coupled observations/modelling simulations of the radiative transfer through the biomass burning aerosol plume linked to the record-breaking Australian fires 2019-2020, complementing the work of S22, to estimate the radiative heating in terms of the HR induced in the UTLS by these fires. Description of the

335   hemispheric-scale plume, as well as of the main smoke-charged isolated anticyclonic vortex (Khaykin et al., 2020) associated with these fires, are provided using limb (large-scale plume) and LiDAR (in-vortex) satellite observations. Aerosol observations are used as inputs to a detailed and flexible offline radiative transfer modelling, to produce regional, hemispheric and in-vortex SW and LW HR profiles estimates. Different hypotheses on the plume evolution have been considered, mirrored by the evolving unmeasured optical properties of the plume, namely the SSA/absorptivity of the plume

340   and the g/angular distribution of the scattered radiation. As observed also for the TOA and surface RF in S22, we found that large-scale hemispheric HR depend critically on these assumptions, in particular through the dependence of the SW HR. In addition, our results suggest the importance of LW emission in the net HR of biomass burning plumes. For the hemispheric plume, generally SW heating and LW cooling is found for each ageing scenario. The LW cooling is approximately insensitive to the plume ageing while the SW heating has a strong dependency on the aerosol absorptivity, in terms of the

345   SSA, and a very small dependency on the aerosol size, in terms of g. Averaging over all optical/ageing scenarios, our best estimate of the peak hemispheric- and monthly-average net HR is 0.08±0.05 K/d, in February 2020. This value is consistent with the observed ensemble self-lofting of the plume at the hemispheric scale of a few km in 4 months. Our in-vortex HR estimations suggest that radiatively-heated ascending isolated vortices, like the ones observed for the Australian fires 2019-

2020, are likely dominated by small-sized and strongly absorbing BC particles. For this optical scenario, we obtain a very

350 large net HR of 8.4±6.1 K/d in the vortex, with peaks around 15-20 K/d in its denser section around 20-21 km. The in-vortex net HR are consistent with the observed rise of the vortex of about 20 km in a couple of months. Our results confirm the importance of the exceptionally intense Australian fires 2019-2020 in terms of their radiative impacts in the UTLS. It is important to mention that the Australian fires plume is accompanied by other effects on the UTLS composition, including in-vortex ozone depletion and water vapour increases. The effect of these further perturbations on the radiative balance are still

355 to be addressed and are matter of ongoing research.

Data availability

OMPS-LP v2.0 and SAGE data are freely available via the NASA-Earthdata portal (https://search.earthdata.nasa.gov/search). The CALIOP data v3.41 are freely available from the NASA LARC website at: https://doi.org/10.5067/CALIOP/CALIPSO/CAL_LID_L1-VALSTAGE1-V3-41.

360 ## Acknowledgments

This research has been supported by the Agence Nationale de la Recherche (ANR, grant no 21-CE01-0007-01, ASTuS) and the Centre National d'Etudes Spatiales (CNES, grant CNES/TOSCA/EECLAT). The providers of the libRadtran suite (http://www.libradtran.org/) are gratefully acknowledged.

Authors contributions

365 P.S. designed the study and ran the radiative simulations. R.B. and J.C. helped with SAGE/OMPS and CALIOP input data. A.P and B.L. helped with the interpretation of the radiative/dynamical processes in the plumes. All authors participated to the discussion of the results. P.S. wrote the manuscript and all authors participated to its revision and the editing.

Competing interests

Some authors are members of the editorial board of ACP. The peer-review process was guided by an independent editor, and

370 the authors have also no other competing interests to declare.

References

Anderson, G. P., Clough, S. A., Kneizys, F. X., Chetwynd, J. H., and Shettle, E. P.: AFGL atmospheric constituent profiles (0–120 km), available at: http://www.dtic.mil/cgi-bin/GetTRDoc?AD=ADA175173 (last access: 2 June 2016), 1986.

Andersson, S., Martinsson, B., Vernier, JP. et al. : Significant radiative impact of volcanic aerosol in the lowermost stratosphere., Nat. Commun. 6, 7692, https://doi.org/10.1038/ncomms8692, 2015.

Brown, H., Liu, X., Pokhrel, R. et al. : Biomass burning aerosols in most climate models are too absorbing, Nat. Commun. 12, 277, https://doi.org/10.1038/s41467-020-20482-9, 2021.

Boer, M.M., Resco de Dios, V., and Bradstock, R.A.; Unprecedented burn area of Australian mega forest fires., Nat. Clim. Chang. 10, 171–172, https://doi.org/10.1038/s41558-020-0716-1, 2020.

Brown, H., Liu, X., Pokhrel, R., Murphy, S., Lu, Z., Saleh, R. Mielonen, T., Kokkola, H., Bergman, T. Myhre, G., Skeie, R. B., Watson-Paris, D., Stier, P., Johnson, B., Bellouin, N., Schultz, M., Vakkari, V., Beukes, J. P., van Zyl, P. G., Liu, S., and Chand, D.: Biomass burning aerosols in most climate models are too absorbing, Nat. Commun. 12, 277, https://doi.org/10.1038/s41467-020-20482-9, 2021.

Burton, S. P., Ferrare, R. A., Vaughan, M. A., Omar, A. H., Rogers, R. R., Hostetler, C. A., and Hair, J. W.: Aerosol classification from airborne HSRL and comparisons with the CALIPSO vertical feature mask, Atmos. Meas. Tech., 6, 1397–1412, https://doi.org/10.5194/amt-6-1397-2013, 2013.

Canadell, J.G., Meyer, C.P., Cook, G.D. et al.: Multi-decadal increase of forest burned area in Australia is linked to climate change., Nat Commun 12, 6921, https://doi.org/10.1038/s41467-021-27225-4, 2021

Dahlback, A. and Stamnes, K.: A new spherical model for computing the radiation field available for photolysis and heating at twilight, Planet. Space Sci., 39, 671–683, 1991.

Duane, A., Castellnou, M., and Brotons, L.: Towards a comprehensive look at global drivers of novel extreme wildfire events., Climatic Change 165, 43, https://doi.org/10.1007/s10584-021-03066-4, 2021

Emde, C., Buras-Schnell, R., Kylling, A., Mayer, B., Gasteiger, J., Hamann, U., Kylling, J., Richter, B., Pause, C., Dowling, T., and Bugliaro, L.: The libRadtran software package for radiative transfer calculations (version 2.0.1), Geosci. Model Dev., 9, 1647–1672, https://doi.org/10.5194/gmd-9-1647-2016, 2016.

Fernald, F. G. Analysis of atmospheric lidar observations: some comments. Appl. Opt. 23, 652–653, 1984.

Heinold, B., Baars, H., Barja, B., Christensen, M., Kubin, A., Ohneiser, K., Schepanski, K., Schutgens, N., Senf, F., Schrödner, R., Villanueva, D., and Tegen, I.: Important role of stratospheric injection height for the distribution and radiative forcing of smoke aerosol from the 2019–2020 Australian wildfires, Atmos. Chem. Phys., 22, 9969–9985, https://doi.org/10.5194/acp-22-9969-2022, 2022. Hirsch, E. and Koren, I.: Record-breaking aerosol levels explained by smoke injection into the stratosphere, Science, 371, 6535, https://doi.org/10.1126/science.abe1415, 2021.

Kablick, G. P., Allen, D. R., Fromm, M. D., and Nedoluha, G. E.: Australian pyroCb smoke generates synoptic-scale stratospheric anticyclones. Geophys. Res. Lett. 47, e2020GL088101, https://doi.org/10.1029/2020GL088101, 2020.

Khaykin, S., Legras, B., Bucci, S., Sellitto P., et al.: The 2019/20 Australian wildfires generated a persistent smoke-charged vortex rising up to 35 km altitude, Commun. Earth Environ. 1, 22, https://doi.org/10.1038/s43247-020-00022-5, 2020.

Kloss, C., Sellitto, P., von Hobe, M., Berthet, G., Smale, D., Krysztofiak, G., Xue, C., Qiu, C., Jégou, F., Ouerghemmi, I., and Legras, B.: Australian Fires 2019–2020: Tropospheric and Stratospheric Pollution Throughout the Whole Fire Season, Front. Environ. Sci., 9, 652024, https://doi.org/10.3389/fenvs.2021.652024, 2021.

Hummel, J.R., Shettle, E.P. and Longtin, D.R., "A New Background Stratospheric Aerosol Model for Use in Atmospheric
410 Radiation Models", AFGL-TR-88-0166, Air Force Geophysics Laboratory, Hanscom AFB, MA, August, 1988.

Kremser, S., et al., Stratospheric aerosol—Observations, processes, and impact on climate, Rev. Geophys., 54, 278– 335, doi:10.1002/2015RG000511, 2016.

Lestrelin, H., Legras, B., Podglajen, A., and Salihoglu, M.: Smoke-charged vortices in the stratosphere generated by wildfires and their behaviour in both hemispheres: comparing Australia 2020 to Canada 2017, Atmos. Chem. Phys., 21,
415 7113–7134, https://doi.org/10.5194/acp-21-7113-2021, 2021.

Papagiannopoulos, N., Mona, L., Amodeo, A., D'Amico, G., Gumà Claramunt, P., Pappalardo, G., Alados-Arboledas, L., Guerrero-Rascado, J. L., Amiridis, V., Kokkalis, P., Apituley, A., Baars, H., Schwarz, A., Wandinger, U., Binietoglou, I., Nicolae, D., Bortoli, D., Comerón, A., Rodríguez-Gómez, A., Sicard, M., Papayannis, A., and Wiegner, M.: An automatic observation-based aerosol typing method for EARLINET, Atmos. Chem. Phys., 18, 15879–15901,
420 https://doi.org/10.5194/acp-18-15879-2018, 2018.

Podglajen, A., Legras, B., Lapeyre, G., Brémaud, V., Zeitlin, V., Plougonven, R., Sellitto, P., Dynamics of diabatically-forced (heated and cooled) anticyclones from wildfires and volcanic eruption plumes in the stratosphere, submitted to QJRMS, 2023

Sellitto, P., Belhadji, R., Kloss, C., and Legras, B.: Radiative impacts of the Australian bushfires 2019–2020 – Part 1: Large-
425 scale radiative forcing, Atmos. Chem. Phys., 22, 9299–9311, https://doi.org/10.5194/acp-22-9299-2022, 2022.

Solomon, S. et al., On the stratospheric chemistry of midlatitudewildfire smoke, PNAS 119, 10 e2117325119, 2022.

Sutherland, R. A. and Khanna, R. K., Optical Properties of Organic-based Aerosols Produced by Burning Vegetation, Aerosol Science and Technology, 14:3, 331-342, DOI: 10.1080/02786829108959495, 1991

Yu, P., Davis, S. M., Toon, O. B., Portmann, R. W., Bardeen, C. G., Barnes, J. E., Telg, H., Maloney, C., and Rosenlof, K.
430 H.: Persistent stratospheric warming due to 2019–2020 Australian wildfire smoke, Geophys. Res. Lett., 48, e2021GL092609, https://doi.org/10.1029/2021GL092609, 2021.